Supplemental Information

Filler Effects Inspired High Performance Polyurethane Elastomer Design: Segment Arrangement Control

Jiaxin Shi[# 1], Tianze Zheng[# 1], Zhiqi Wang[1], Pujin Wang[1], Hongkun Yang[2], Jinjing Guo[1], Dong Wang[2], Baohua Guo[1], Jun Xu[* 1]

1 Advanced Materials Laboratory of Ministry of Education (MOE), Department of Chemical Engineering, Tsinghua University, Beijing, 100084, China

2 State Key Laboratory of Organic−Inorganic Composites & Beijing Key Laboratory of Advanced Functional Polymer Composites, Beijing University of Chemical Technology, Beijing 100029, China

E-mail: jun-xu@mail.tsinghua.edu.cn

ORCID: 0000-0003-2345-0541

Experimental Section

Materials

Polyoxytetramethylene (PTMEG, Alladin, M_n=650/850/1000 g mol^{-1}) was dried under vacuum at 110°C prior to use. Isophorone diisocyanate (IPDI, 99%), butanediol (BDO, 99%), dibutyltindilaurate (DBTDL, 98%) and 1,4-dioxane (ultra dry, 99%) were purchased from Admas-Beta. Acetone d_6 was purchased from Energy Chemical. All reagents were used as received except PTMEG.

Pre-polymerization of PTMEG and IPDI

Fifteen types of prepolymers were prepared using a one-pot process, and the feeding ratios for each sample are presented in Table S1. In a representative procedure, 10.00g (10mmol) of PTMEG 1000, 1.11g (5mmol) of IPDI, and 0.02g of DBTDL (0.2 wt% of PTMEG) were mixed. The mixture was then heated to 80°C and stirred for three hours. The GPC results for the prepolymer can be found in Table S1, while the ^{1}H NMR results are displayed in Figure S1. Additionally, the shear viscosity data is illustrated in Figure S4.

Preparation of TPU by chain extension of prepolymers

After synthesizing the prepolymer, a solution of IPDI and BDO in 10ml of 1,4-dioxane was added to the prepolymer at 80°C and stirred for a few minutes. The resulting mixture was then degassed under vacuum to remove any bubbles. Subsequently, the mixture was poured onto a Teflon plate and cured for 12 hours at 80°C under dry conditions. To obtain a transparent sheet, the polymer was further dried under vacuum at 60°C for approximately 48 hours. The feeding ratios and GPC results for different samples can be found in Table S2. Additionally, the FTIR results are presented in Figure S3.

General characterization

Fourier transform infrared (FTIR) spectra were collected on a Nicolet 6700 FT-IR spectrophotometer equipped with a deuterated triglycine sulfate detector. Each sample was cast onto a KBr plate to obtain a thin film. The transmission spectra were collected with an average of 16 scans for each run at a resolution of 4 cm^{-1} in the range of 4000−500 cm^{-1}. Differential scanning calorimetry (DSC) measurement was conducted on a DSC 250 (TA Instrument) with a heating and cooling rate of 10 °C/min under nitrogen atmosphere. Dynamic mechanical analysis (DMA) was carried out on an DMA Q850 apparatus (TA Instrument) in a tension film mode at temperatures ranging from -80 to 150 °C with a heating rate of 3 °C min^{-1}. The maximum strain was 0.05% and the frequency was 1 Hz. Rheological tests are carried out on an Anton Paar MCR301 rheometer in a parallel-plate mode, each sample was first equilibrated at a set temperature for 5 minutes. Dumbbell-shaped specimens for tensile tests were cut from cast sheets using a standard bench-top die according to GB/T-528 (ca. 1mm(thickness) × 2mm(width) × 35mm(length) and a gauge length of 10 mm). Tensile tests were conducted on a JinJian UTM-1432 tensile tester equipped with a 500 N load cell at 25°C. Small Angle X-ray Scattering (SAXS) measurement was conducted on a Xenocs Xeuss 1.0. Atomic force microscopy (AFM) measurements were performed in tapping mode on a Bruker MultiMode 8 AFM under ambient conditions. OMCL-AC240TS-R3 cantilevers (OLYMPUS Micro Cantilevers) with a nominal resonance frequency of ~70 kHz and a spring constant of ~2 N/m were used to image the sample surface at a setpoint ratio of ~0.85. In situ WAXS and SAXS was carried on Xenocs Xeuss 3.0.

Self-healing test

In the self-healing test of scratches, the sample with thickness of ca. 1mm was initially put on a glass slide and then scratched by a razor. To observe the self-healing ability of 850-3, the sample was heated at 120 °C for a period and the images under microscope were taken.

In the uniaxial self-healing test, the dumbbell-shaped specimen was cut in half with a razor, then the

two pieces were gently brought into contact for 10 s and put into an oven with desiccant to heal under different temperatures without external force. After self-healing, the sample was cooled to room temperature. At last, the healed specimen was tested on tensile tester.

SAXS analysis

The peak position is associated with the interdomain spacing:

$$d=2\pi/q_{max}$$

where d represents the three-dimensional mean of the scatterer volume. In the case of stacked layered structures, the one-dimensional spacing is typically determined by defining q_{max} as the q value at the maximum intensity of $I(q)q^2$-q. Otherwise, q_{max} is generally defined as the value of q at the maximum intensity of I(q)-q. The AFM images reveal that the phase structure of all TPU samples does not exhibit a stacked layer configuration. Therefore, the scattering object size, i.e., microphase size, can be calculated from the peak positions of I(q)-q.

Since the phase separation ratio needs to be calculated, it is necessary to perform an absolute intensity correction. The basic formula is:

$$I_{rel}(q) = \frac{I_0}{A_i} A_s d T_s I_{abs}(q) \Delta\Omega t$$

Where $I_{rel}(q)$ is the relative scattering intensity (counts/s), I_0 is the incident light intensity (counts/s), A_i is the irradiation area of the incident beam at the sample position, A_s is the area where the sample is illuminated by the beam, d is the thickness of the sample, T_s is the transmittance of the sample, $I_{abs}(q)$ is the absolute scattering intensity of the sample, also known as the micro dispersion cross-section per unit volume (cm^{-1}), t is the exposure time, and $\Delta\Omega$ is the solid angle clamped by a pixel on the detector. where the solid angle is defined as:

$$\Delta\Omega = \frac{p_1 p_2 L_0 / L_p}{L_p^2}$$

p_1 and p_2 are the size of a pixel horizontally and vertically, L_0 is the distance from the sample to the detector, and L_p is the distance from the sample to each pixel.

If the sample is large enough that the incident beam hits the sample at the sample, then $A_i = A_s$. Then the absolute scattering intensity of the sample is:

$$I_{abs}(q) = \frac{I_{rel}(q)}{I_0 d T_s t} \frac{L_p^3}{p_1 p_2 L_0}$$

The parameters of the SAXS instrument we use are: p_1 and p_2 at 172μm, t for 20 min, and L_0 for 2527 mm. Since the scattering angle is small, L_0 is approximately equal to L_p.

The SAXS data were corrected for background noise and thermal density fluctuations. Since high-q data are available, a q-dependent background correction was performed via the method of Ruland. This involves fitting the high-q data (in the Porod region) to an exponential function by adjusting constants a and b:

$$I_b(q) = a e^{bq^2}$$

The background scatter [$I_b(q)$] is calculated over all q and then subtracted from the raw intensities.

The theoretical variance is calculated based on the assumption of complete separation between the hard and soft segments and is defined as:

$$\Delta\eta_c{}^2 = \phi_{hs}\phi_{ss}(\eta_{hs} - \eta_{ss})^2$$

ϕ_{hs} represents the volume fraction of the hard segment, which includes IPDI and BDO, while ϕ_{ss} represents the volume fraction of the soft segment, including PTMEG. The electron densities of the hard and soft segments, denoted as η_{hs} and η_{ss}, respectively, can be calculated using the group contribution

method. It should be noted that in this analysis, we also consider the "short hard segment" as part of the hard segment, despite its weak microphase separation ability. Since the chemical composition of TPUs with different sequence distributions is identical, the $\Delta\eta_c{}^2$ value for each series of TPUs is the same. Specifically, the $\Delta\eta_c{}^2$ values are 2.730×10^{-3} (mol $e^-/cm^3)^2$ for the 650 series, 2.635×10^{-3} (mol $e^-/cm^3)^2$ for the 850 series, and 2.526×10^{-3} (mol $e^-/cm^3)^2$ for the 1000 series.

In fact, the soft and hard segments are not completely incompatible, resulting in an experimental electron density variance that is much smaller than the theoretical value. This experimental variance can be determined from the SAXS results and is defined as:

$$\Delta\eta_c{}^{2\prime} = cQ = c\int_0^{+\infty} I(q)q^2dq$$

Q is the integral invariant and c is:

$$c = \frac{1}{2\pi^2 i_e N_A{}^2} = 1.76\times10^{-24} mol^2/cm^2$$

i_e represents Thompson's constant ($7.94\times10^{-26}cm^2$), and N_A is the Avogadro constant. $\Delta\eta_c{}^{2\prime}/\Delta\eta_c{}^2$ represents the microphase separation ratio. Additionally, the phase interface diffusion and the mixing of soft and hard segments can also be determined from SAXS. Assuming that the interface follows an S-shaped gradient, the relationship between the corrected scattering intensity and the interface parameters can be described as:

$$I(q) = I_{id}(q)(1-\sigma^2q^2)$$

In the large q region, $I_{id}(q)$ represents the ideal scattering intensity, and σ denotes the diffusion interface layer thickness. $I_{id}(q)$ follows Porod's law, and therefore, the above equation can be expressed as:

$$I(q) = \frac{K}{q^4}(1-\sigma^2q^2)$$

Hence, the diffusion interface thickness (σ) can be determined by calculating the slope ($K\sigma^2$) and intercept (K) of the fitted line in the large q region of the $q^4I(q)$-q^2 plot. Moreover, to eliminate the contribution of the diffusion interface to scattering, the second-order electron density variance can be calculated and defined as:

$$\Delta\eta_c{}^{2\prime\prime} = c\int_0^{+\infty}\frac{I(q)q^2}{H(q)}dq$$

H(q) represents the Fourier transform of the smooth function that characterizes the shape and size of the diffusion interface, given by $H(q) = \exp(-\frac{\sigma^2q^2}{2})$. Consequently, $\frac{\Delta\eta_c{}^{2\prime\prime}}{\Delta\eta_c{}^{2\prime}} - 1$ serves as a measure of the segment mixing, while $\frac{\Delta\eta_c{}^2}{\Delta\eta_c{}^{2\prime\prime}} - 1$ provides a measure of the diffuse interface.

Calculation of the Flory-Huggins parameter by all-atom molecular dynamics simulations

Structure one representing the hard segment and structure two representing the soft segment are calculated separately. The simulation system consisted of 80 molecules. The simulations were carried out using the Forcite module of the Materials Studio (Accelrys inc., San Diego) with COMPASSII force field, and the atomic point charges were calculated by the Gasteiger method. The initial configurations of simulation systems were constructed by randomly distributing the molecules in simulation cells using the Amorphous Cell module of the Materials Studio. The structures were annealed via following steps. First, annealed at 500K for 2ns under NPT ensemble at one bar pressure. Second, a linear cooling process from 500 K to 300 K for 2ns. Third, annealed at 300K for 2ns under NPT ensemble at one bar pressure. Finally, append 1ns under NVT. The solubility parameter of structure one is 21.316 $(J/cm^3)^{1/2}$, and the

solubility parameter of structure two is 18.582 $(J/cm^3)^{1/2}$. The Flory-Huggins parameter calculated by

$$\chi_{ij} = \frac{V}{RT}(\delta_i - \delta_j)^2$$

Where V is the bead molar volume, R is the gas constant, δ_i and δ_j are the solubility parameter of particles i and j. The calculated χ is 0.98, significantly smaller than the PTMEG-MDI-BDO system with strong microphase separation, which has a χ of approximately 3.[1]

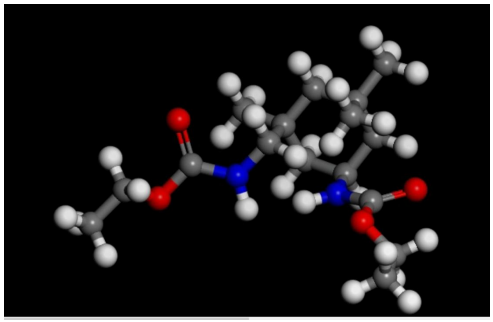

Scheme S1. Structure one representing the hard segment. The white is H atom, gray is C atom, red is O atom, blue is N atom.

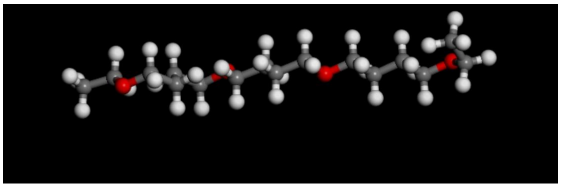

Scheme S2. Structure two representing the soft segment. The white is H atom, gray is C atom, red is O atom.

Stochastic polymerization simulation

To obtain the sequence structure achieved through the prepolymerization-chain extension method, we conducted simulations using a Home-Made program. The simulation involved three reactive monomers: IPDI, BDO, and PTMEG. The isocyanate groups at the ends of IPDI and the hydroxyl groups at the ends of BDO and PTMEG react to form urethane groups, connecting the repeating units.

In the simulations, we assumed that the system was homogeneous throughout the reaction, meaning that the functional groups at the ends of the monomers or polymers had the same reactivity. This implies that the probability of a reaction occurring was the same for all functional groups.

Firstly, we performed pre-polymerization simulations by adding PTMEG and IPDI to the system. Specifically, 12,000 PTMEG molecules were added in each reaction, and the number of IPDI was calculated based on the proportions used in the actual experiment. The terminal functional groups of PTMEG and IPDI then randomly reacted, forming oligomers. The simulation stopped when all the isocyanate groups had reacted.

Next, we proceeded with the chain-extension stage by adding BDO and the remaining IPDI to the system according to the experimental proportions. Random reactions were simulated until the conversion ratio of the isocyanate groups reached 99.5%. In the actual experiment, due to factors such as weighing accuracy and moisture in the air, it was not possible for all the isocyanate groups to participate in the polymerization process. Therefore, we chose to stop the simulation when the conversion ratio reached 99.5% and not higher. Additionally, small molecules or oligomers with a molecular weight below 200Da

were removed from the system, as they would have been eliminated during vacuum drying in the actual experiment.

The molecular weight distribution of the entire polymer chain and the molecular weight distribution of the hard segment were calculated. Five parallel experiments were conducted with different random number seeds. It is important to note that the chain segment formed by a single IPDI and two PTMEGs was not considered as it is not easily microphase separated from other soft segments. Only consecutive IPDIs connected by BDO were counted as hard segments.

DPD simulation

The molecular chains were placed in a simulation box under periodic boundary conditions using random growth, and the density of the system was set to 3.0, which is commonly used for DPD simulations. The temperature was set to 1.0. We performed an initial simulation of 100,000 steps using a time step of 0.001, followed by a longer simulation of 1,000,000 steps using a time step of 0.01. We verified that this simulation duration was sufficient, as longer simulations did not result in further changes in the microphase structure and radial distribution function (RDF). During the simulation, the same parameters were used for all H_0 beads. However, when calculating the RDF and visualizing the system, we further divided the H_0 beads into two types: "short hard segments" (I) without the chain extender BDO, and "long hard segments" (H) containing BDO. The RDF calculations were performed separately for H-H and I-I to study the differences between the long and short hard segments. In the visualization, H beads were represented in red, while I beads were represented in purple. The DPD simulation was conducted using the LAMMPS open-source software, and visualization and RDF calculations were performed using the OVITO software.

Statistical Analysis of the Strong Hard Domains

Given the 3D coordinates of all the hard beads in the simulation box, a naïve way to define the density of hard beads is:

$$\rho'(\boldsymbol{r}) = \sum_{i=1}^{n} \delta(\boldsymbol{r} - \boldsymbol{r}_i)$$

where δ is the Dirac delta function, $\boldsymbol{r}_i$ is the coordinate of the i[th] hard bead. In the simulation, each bead occupies a point in space, so the density is discrete. Actually, each bead represents a group of atoms, which means the density should larger than zero in the neighborhood of one bead. Therefore, the density is calculated by the convolution of $\rho'(\boldsymbol{r})$ and a kernel function $\kappa(\boldsymbol{r})$:

$$\rho(\boldsymbol{r}) = \kappa * \rho'(\boldsymbol{r}) = \sum_{i=1}^{n} \kappa(\boldsymbol{r} - \boldsymbol{r}_i).$$

Specifically, $\kappa(\boldsymbol{r})$ is a truncated Gaussian distribution:

$$\kappa(\boldsymbol{r}) = \begin{cases} \dfrac{\exp\left(-\frac{\|r\|_2^2}{2\sigma^2}\right)}{\int_0^{r_c} \exp\left(-\frac{\|r\|_2^2}{2\sigma^2}\right) d\boldsymbol{r}}, \|\boldsymbol{r}\|_2 < r_c \\ 0, \quad \|\boldsymbol{r}\|_2 \geq r_c \end{cases},$$

where r_c is the cutoff distance and σ is a parameter which controls the shape of the kernel function. They were set to 2.0 and 1.0 in the reduced unit respectively.

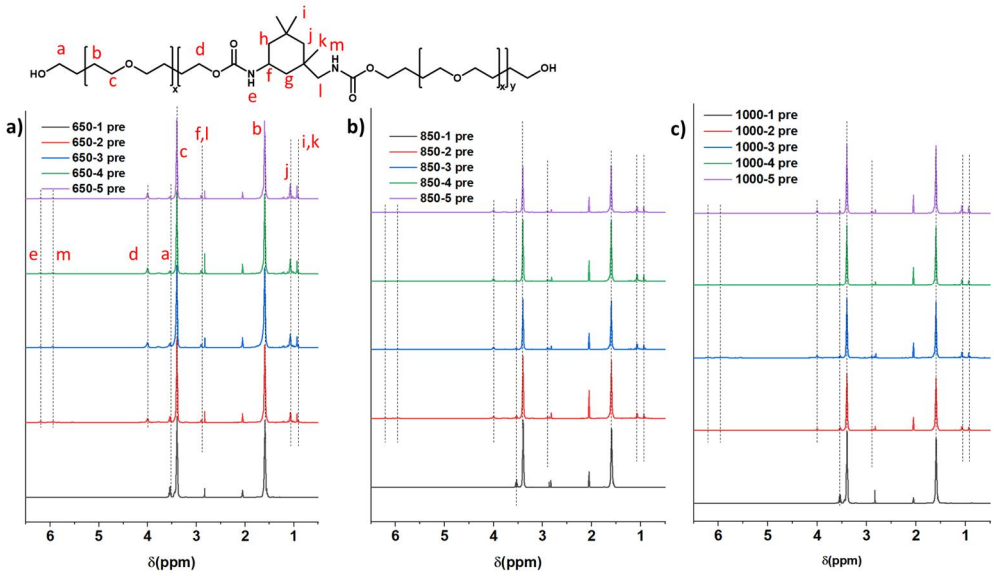

Figure S1. ^{1}H NMR spectra of prepolymers.

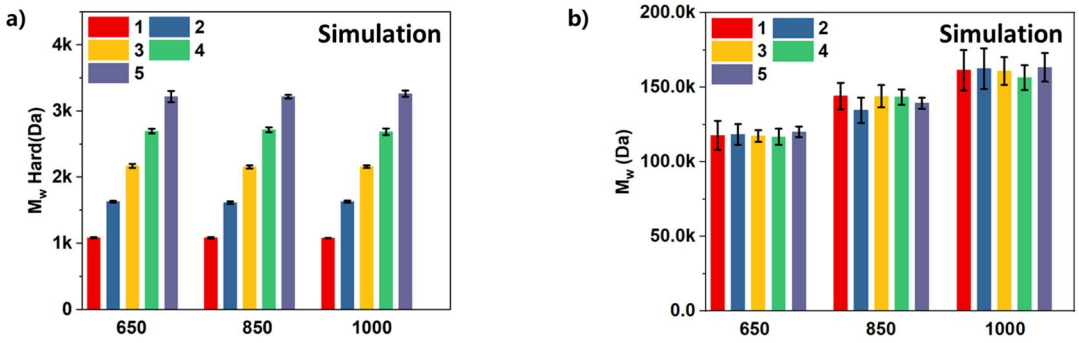

Figure S2. The M_w of (a) the long hard segment (hard segment including BDO) and (b) TPU polymer calculated by stochastic reaction simulation.

Table S1. Feed ratio and molecular weight of prepolymers

Samples	Molar ratio[a])	M_n(g/mol)	M_w(g/mol)	PDI
650-1 pre	1:0	648	1107	1.71
650-2 pre	2:1	1529	3685	2.40
650-3 pre	3:2	2397	4188	1.75
650-4 pre	4:3	3250	5830	1.79
650-5 pre	5:4	4111	7638	1.86
850-1 pre	1:0	857	1976	2.31
850-2 pre	2:1	1966	3711	1.89
850-3 pre	3:2	2954	5760	1.90
850-4 pre	4:3	4099	7493	1.83
850-5 pre	5:4	5133	9717	1.89
1000-1 pre	1:0	1024	2143	2.09
1000-2 pre	2:1	2265	6003	2.65
1000-3 pre	3:2	3508	6247	1.78
1000-4 pre	4:3	4633	8381	1.81
1000-5 pre	5:4	5983	11409	1.91

[a)] The molar ratio of PTMEG : IPDI.

Table S2. Feed ratio and molecular weight of TPUs

Samples	Molar ratio[a]	M_n(g/mol)	M_w(g/mol)	PDI
650-1	1:2:1	1.16×10^5	3.90×10^5	3.35
650-2	1:2:2	8.71×10^4	2.60×10^5	2.99
650-3	1:2:3	9.50×10^4	3.14×10^5	3.31
650-4	1:2:4	1.05×10^5	3.68×10^5	3.50
650-5	1:2:5	9.21×10^4	2.86×10^5	3.11
850-1	1:2:1	1.84×10^5	5.72×10^5	3.11
850-2	1:2:2	2.02×10^5	6.21×10^5	3.07
850-3	1:2:3	2.30×10^5	7.63×10^5	3.32
850-4	1:2:4	2.15×10^5	7.77×10^5	3.15
850-5	1:2:5	2.07×10^5	6.64×10^5	3.21
1000-1	1:2:1	6.19×10^4	1.25×10^5	2.02
1000-2	1:2:2	4.58×10^4	1.18×10^5	2.57
1000-3	1:2:3	5.14×10^4	1.38×10^5	2.69
1000-4	1:2:4	5.29×10^4	1.42×10^5	2.69
1000-5	1:2:5	4.95×10^4	1.32×10^5	2.66

[a)] The molar ratio of Prepolymer: IPDI: BDO.

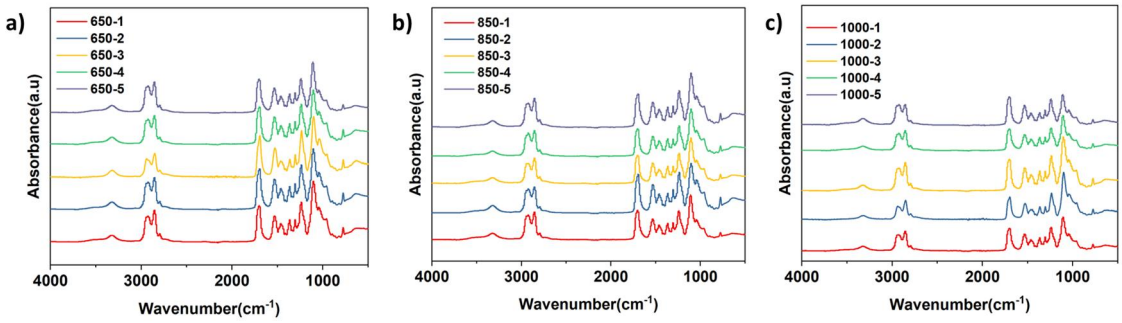

Figure S3. FT-IR spectra of TPUs.

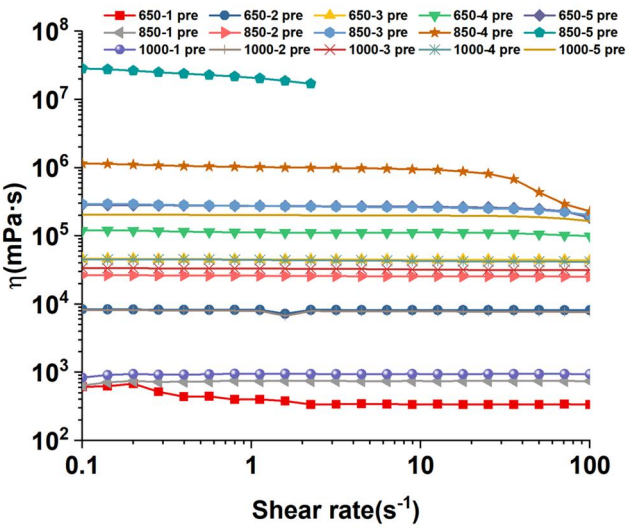

Figure S4. Shear viscosity data of prepolymers.

Table S3. Microphase separation parameters of TPUs.

Sample	Interdomain spacing d [nm]	σ[nm]	Percentage of phase separation [%]	Boundary effect [%]	Intermixing effect [%]
650-1	-	-	5.08	0	94.92
650-2	16.41	0.58	6.95	2.42	90.62
650-3	19.54	0.71	8.51	6.20	85.29
650-4	22.9	0.73	13.62	8.64	77.75
650-5	25.75	0.77	16.57	10.12	73.31
850-1	-	-	3.48	0	96.52
850-2	18.43	0.82	16.16	18.88	64.96
850-3[a)]	21.59	0.86	22.31	16.65	61.04
850-4[a)]	22.44	1.05	20.27	17.93	61.80
850-5[a)]	24.07	1.19	12.42	27.28	60.30
1000-1	-	-	1.94	0	98.06
1000-2	14.09	0.51	6.00	0.36	93.64
1000-3	18.59	0.71	9.88	6.50	83.62
1000-4	20.6	0.74	13.95	8.33	77.72
1000-5	22.44	0.79	15.74	9.14	75.12

a) Some scattering object sizes of 850-4 and 850-5 exceed the detection limit of SAXS, the calculation results cannot reflect the reality.

The degree of microphase separation in the sample 850-4 and 850-5 could not be precisely calculated since the microphase size exceeds the detection limit of SAXS. Apparently, the significant decrease in optical transparency of the two samples (Figure S6) indicates that the microphase sizes have reached hundreds of nanometers, approaching visible light wavelengths. However, the SAXS equipment used in our study is unable to detect scattering objects of this size.

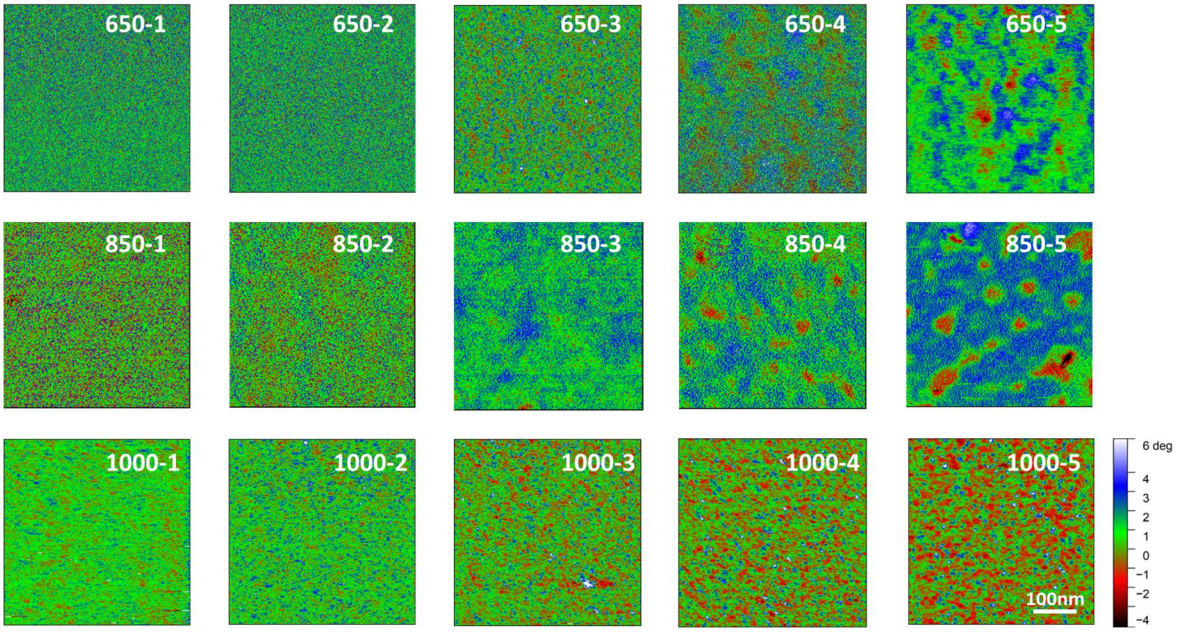

Figure S5. AFM phase images of 15 TPU samples.

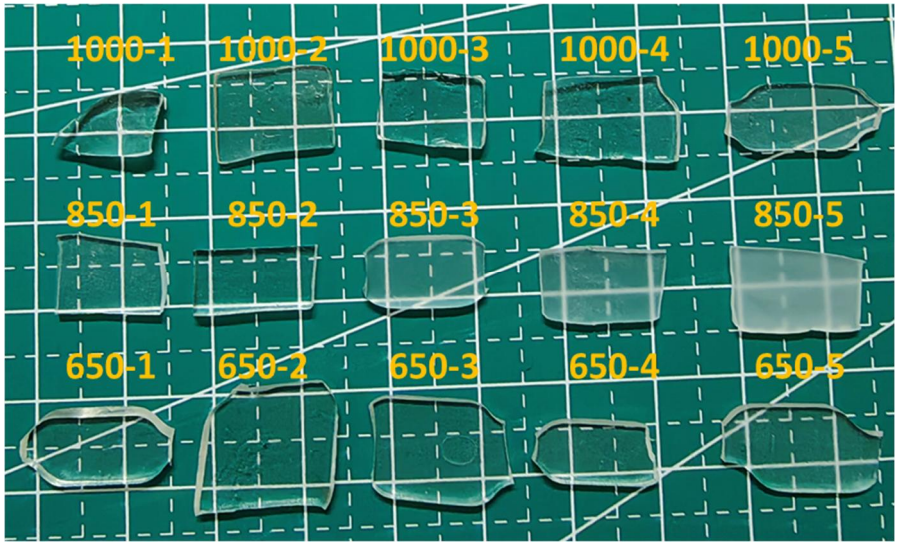

Figure S6. Optical photo of TPUs.

Table S4. Parameters of DPD Simulation

Bond coefficients

Bond type	K [a)]	Equilibrium length
H-H	100.0	1.0
H-S	30.0	1.0
S-S	30.0	1.0
	Angle coefficients	
Angle type	K [a)]	Equilibrium angle
H-H-H	50.0	150°
H-H-S	10.0	150°
H-S-S	10.0	150°
S-H-S	10.0	150°
S-S-S	10.0	150°

[a)] K is the force constant.

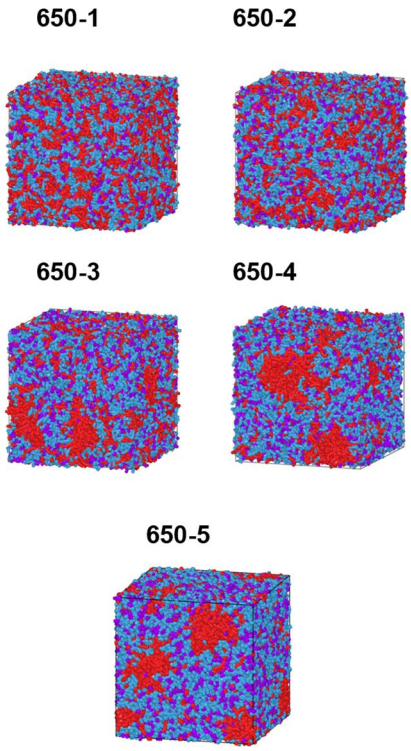

Figure S7. Visualization results of DPD simulation for 650 series TPUs.

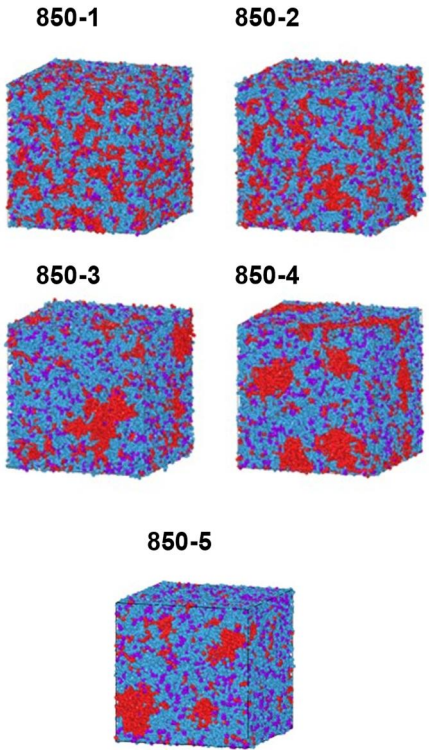

Figure S8. Visualization results of DPD simulation for 850 series TPUs.

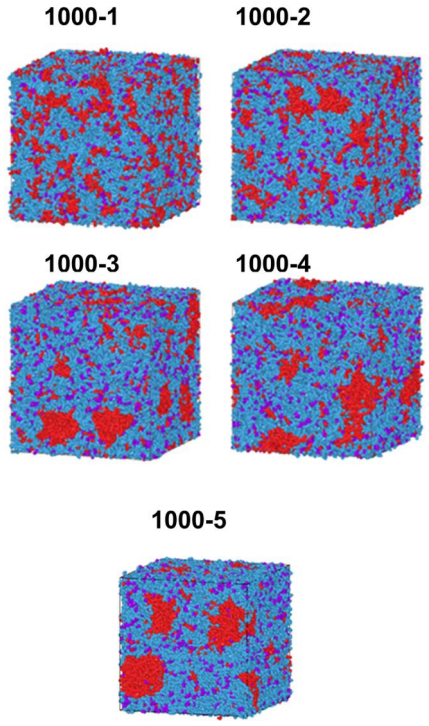

Figure S9. Visualization results of DPD simulation for 1000 series TPUs.

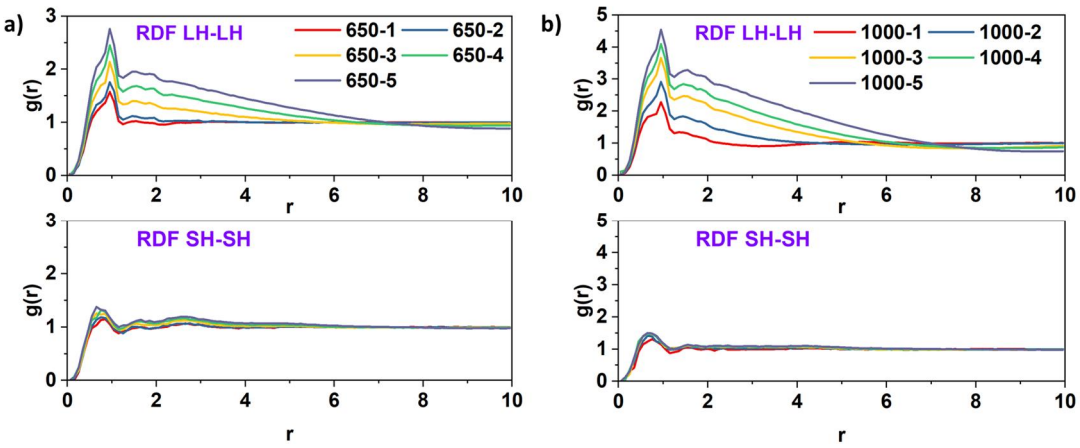

Figure S10. RDF statistics of DPD simulation for (a) 650 series and (b) 850 series.

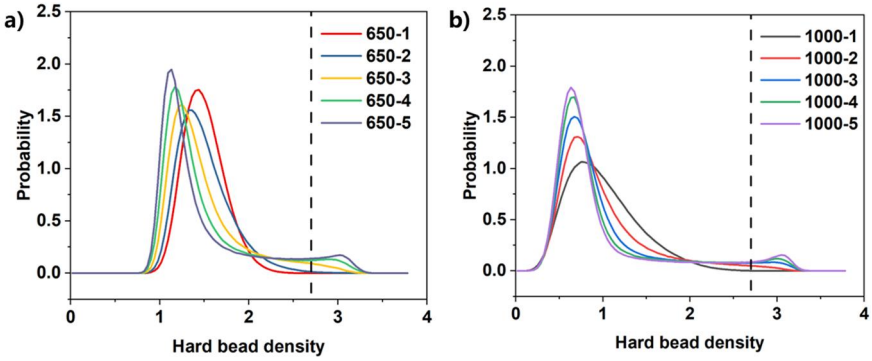

Figure S11. Hard bead packing density distribution for (a) 650 series and (b) 1000 series.

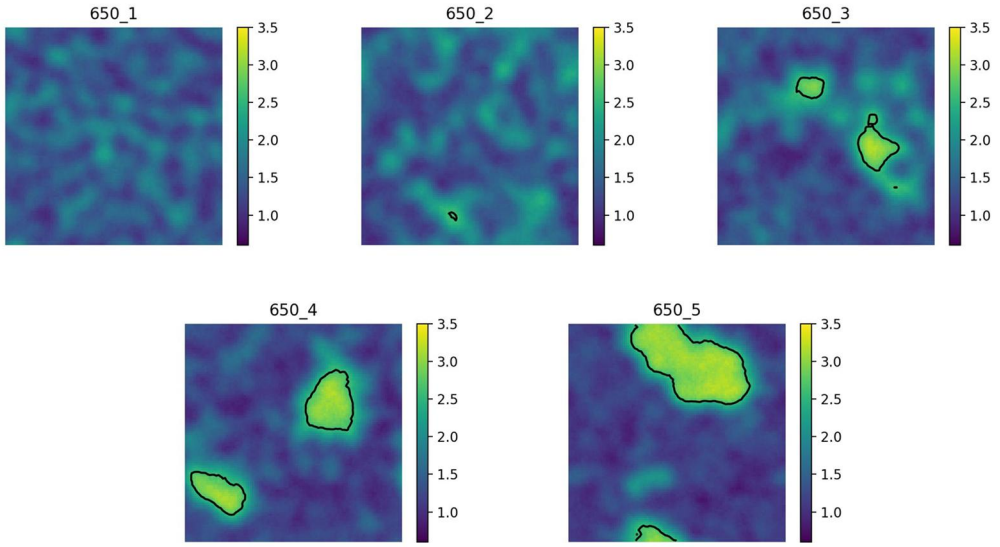

Figure S12. Hard bead density distribution and contour map for 650 series.

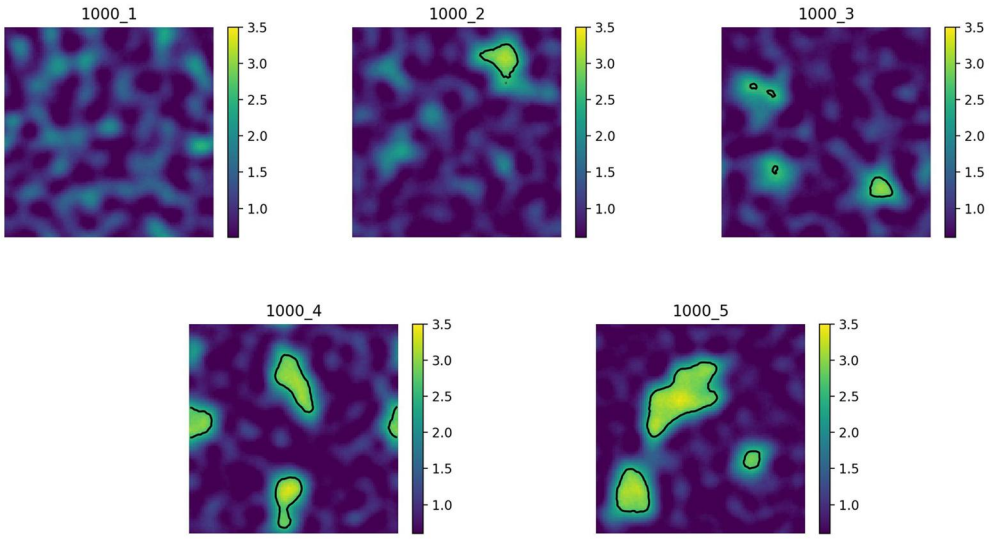

Figure S13. Hard bead density distribution and contour map for 1000 series.

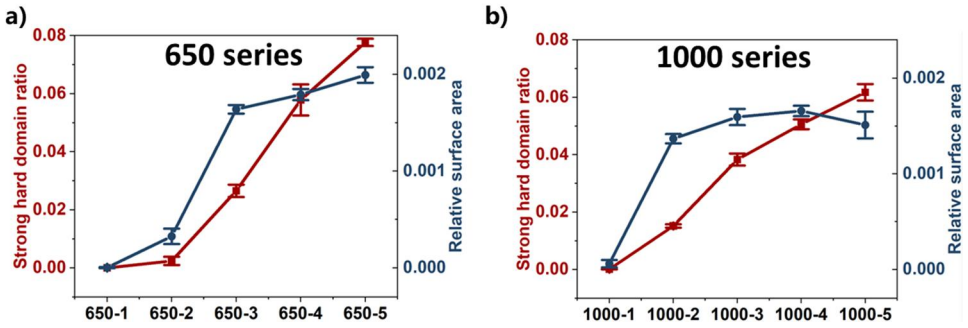

Figure S14. Strong hard domain percentage and relative surface area of (a) 650 series and (b) 1000 series.

Table S5. Mechanical properties of TPUs.

Sample	Ultimate stress (MPa)	Elongation at break (%)	Elastic modulus (MPa)	Toughness (MJ/m^3)
650-1	29.6±2.1	1254±47	2.9±0.5	121.1±12.5
650-2	38.3±2.9	1219±55	4.0±0.8	143.4±16.6
650-3	41.4±3.9	1172±51	5.0±0.7	155.6±19.9
650-4	61.6±5.5	1150±77	8.6±0.9	232.2±32.3
650-5	57.1±5.8	1162±89	8.3±0.8	228.9±31.5
850-1	35.2±3.3	1066±39	4.2±0.4	119.3±10.7
850-2	48.9±3.6	1170±33	5.9±0.3	198.9±14.2
850-3	62.3±1.9	1115±32	8.5±0.3	259.2±11.1
850-4	52.7±2.2	1107±28	6.1±0.5	219.0±13.3
850-5	38.1±3.7	1015±59	5.1±0.4	153.1±12.8
1000-1	-	-	2.0±0.2	-
1000-2	-	-	2.2±0.3	-
1000-3	6.7±0.4	2158±131	2.4±0.2	50.5±5.1
1000-4	16.2±1.2	2073±113	3.2±0.5	118.5±7.7
1000-5	14.0±1.5	1907±138	2.9±0.3	94.8±10.2

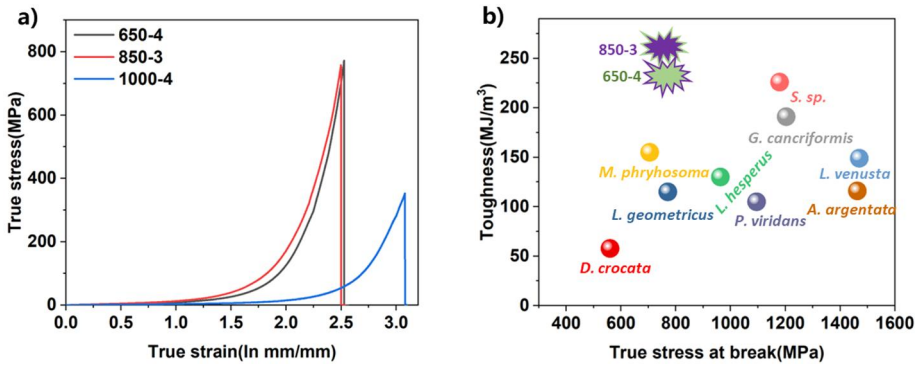

Figure S15. (a) True stress-strain curves of 650-4, 850-3 and 1000-4. (b) Comparison of the true stress at break and toughness among 650-4, 850-3 and the different spider silk.

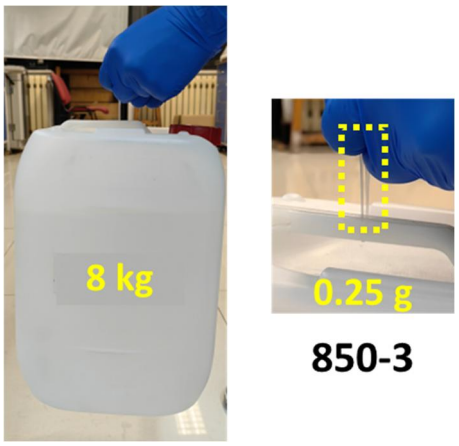

Figure S16. Photographs showing that the 850-3 elastomer strip (0.25 g) can lift a weight of 8 kg.

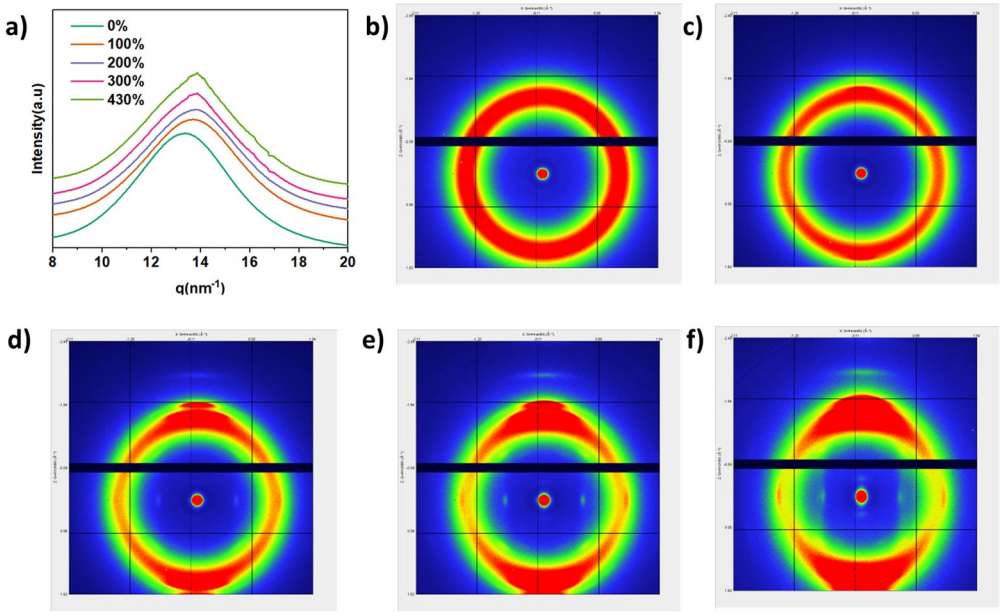

Figure S17. In-situ tensile wide-angle X-ray scattering of 850-3. (a) I(q)~q plots at different strain. 2D WAXS images of 850-3 at (b) 0%, (c) 100%, (d) 200%, (e) 300% and (f) 430% strain.

The remarkable enhancement in both the strength and toughness does not originate from strain-induced crystallization, as evidenced by in-situ wide-angle X-ray scattering during tensile test (Figure S17).

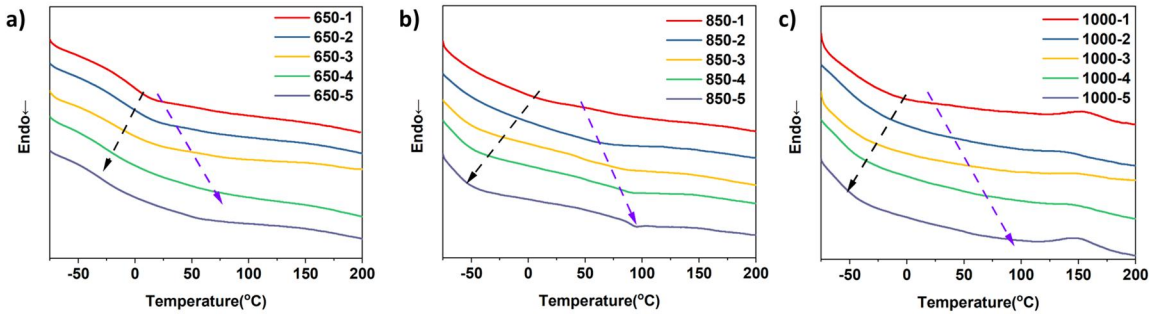

Figure S18. DSC curve of TPUs, the heating rate is 10°C/min.

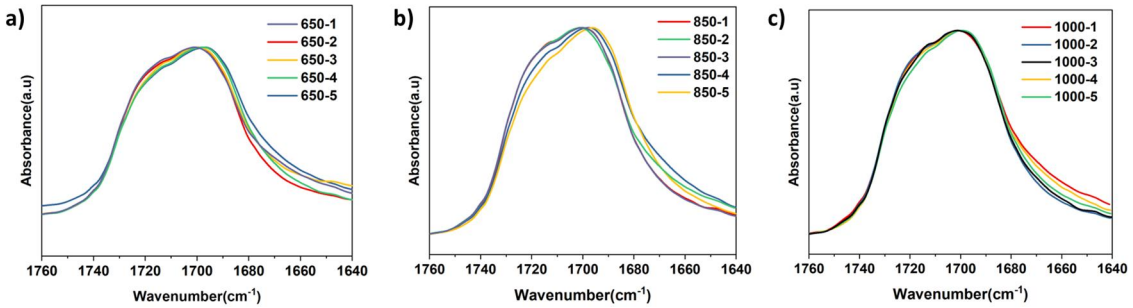

Figure S19. Carbonyl-group FTIR spectra of TPUs (a) 650 series, (b) 850 series and (c) 1000 series.

Table S6. Hydrogen-bonded carbonyl group ratio of TPUs obtained by FTIR.

Sample	Hydrogen-bonded carbonyl group (%)	Free carbonyl group (%)
650-1	51.38	48.62
650-2	53.10	46.90
650-3	53.42	46.58
650-4	54.92	45.08
650-5	55.28	44.72
850-1	52.35	47.65
850-2	52.51	47.49
850-3	52.64	47.36
850-4	54.54	45.46
850-5	57.09	42.91
1000-1	52.96	47.04
1000-2	53.56	46.44
1000-3	53.67	46.33
1000-4	53.84	46.16
1000-5	54.83	45.17

The proportion of hydrogen-bonded carbonyl group was calculated by FTIR spectral peak splitting. The Lorentz curve was used for fitting. The peak of the hydrogen-bonded carbonyl group is 1695 cm^{-1}, and the peak of the free carbonyl group is 1718 cm^{-1}. The peak area as a percentage of the total area is the hydrogen bond/free carbonyl group percentage.

Although the proportion of hydrogen-bonded carbonyl groups increased slightly with the extension of

the hard segment sequence, the increase was too small to account for the large change in mechanical properties. In addition, FTIR detection is only the number of hydrogen bond formation, and cannot reflect the aggregation effect of consecutive hard segments and consecutive hydrogen bonds.

The absorbance of carbonyl groups in FTIR results (Figure S9 and Table S4) reveals that the incorporation of consecutive hard segments does not apparently affect the ratio of hydrogen bonds, which cannot explain the observed significant enhancement in mechanical performance. So, our focus will be on microphase separation.

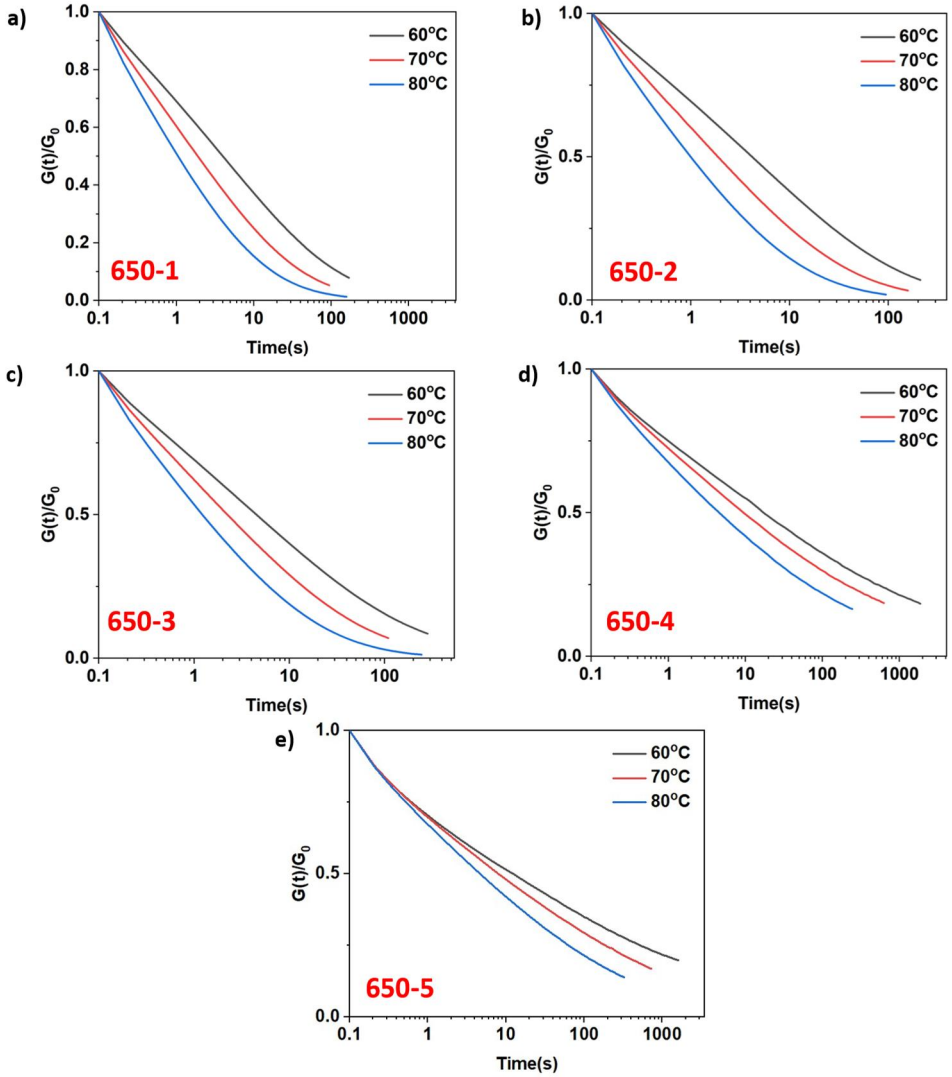

Figure S20. Shear stress relaxation under 1% strain of 650 series TPU. (a) 650-1 (b)650-2 (c)650-3 (d)650-4 (e)650-5

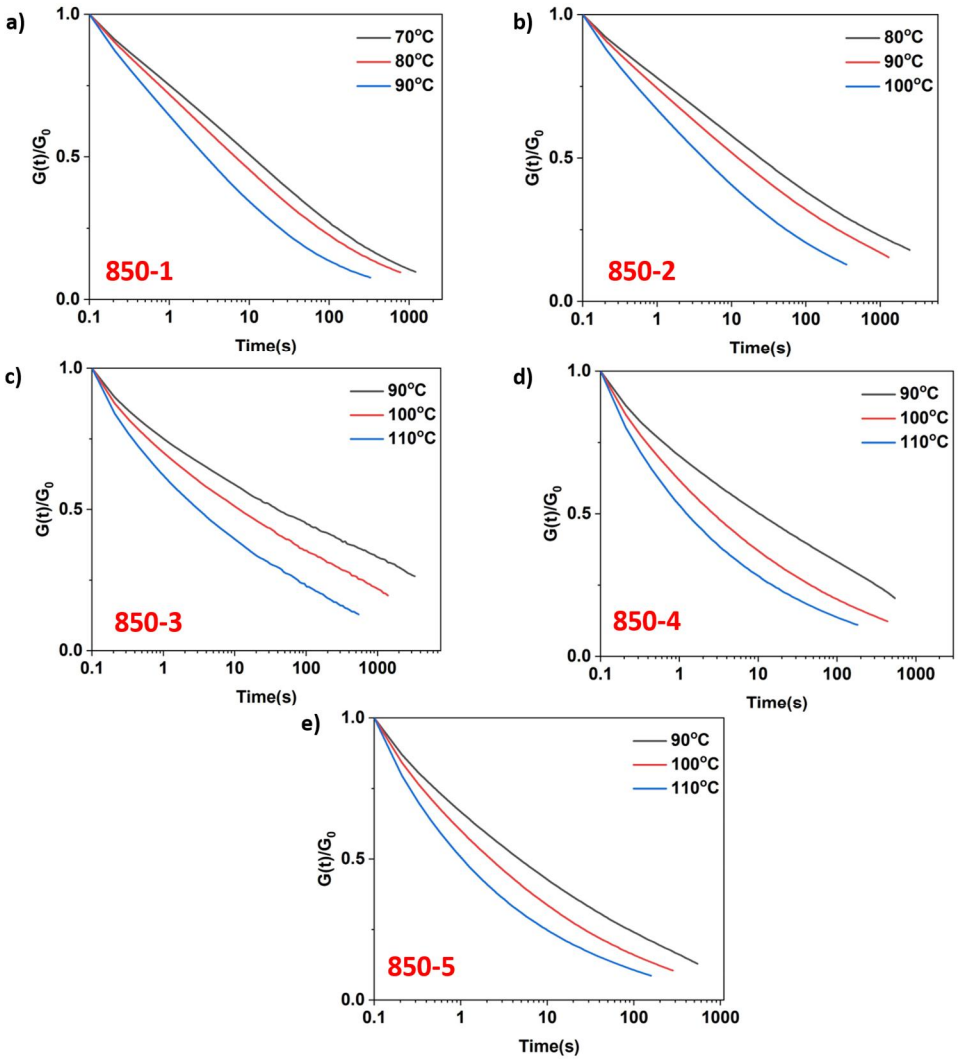

Figure S21. Shear stress relaxation under 1% strain of 850 series TPU. (a) 850-1 (b)850-2 (c)850-3 (d)850-4 (e)850-5

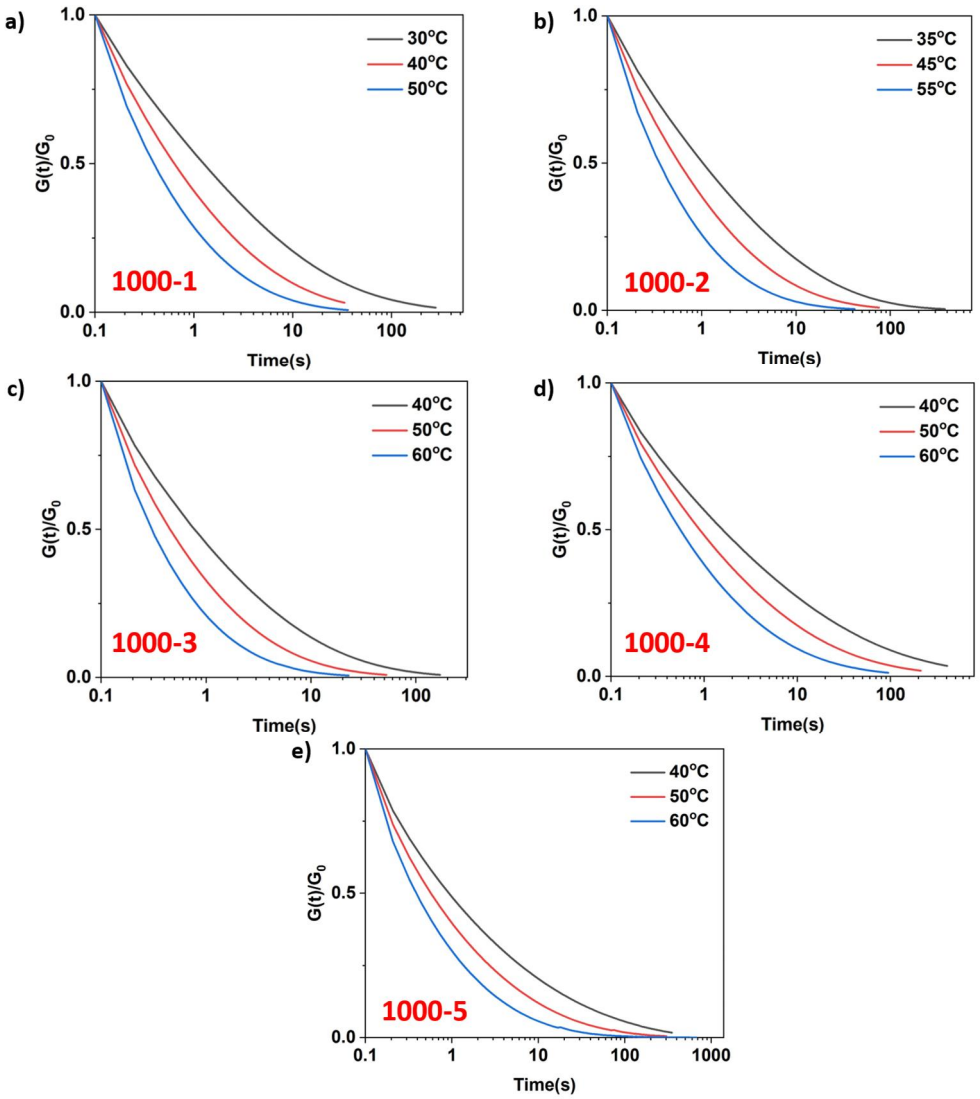

Figure S22. Shear stress relaxation under 1% strain of 1000 series TPU. (a) 1000-1 (b)1000-2 (c)1000-3 (d)1000-4 (e)1000-5

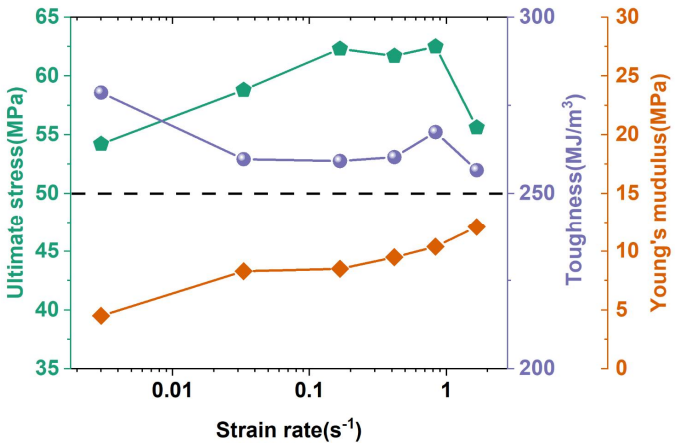

Figure S23. Ultimate stress, toughness, and Young's modulus at different strain rates of 850-3.

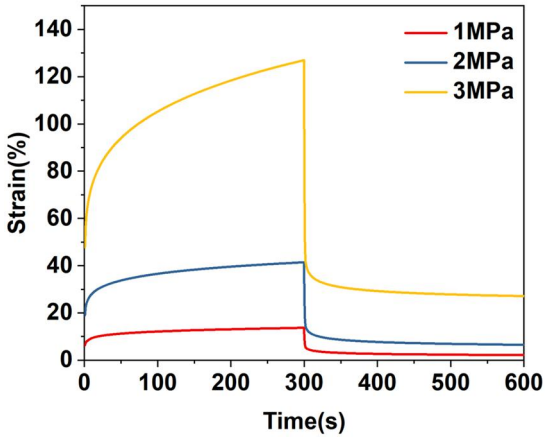

Figure S24. Creep-recovery behaviors of 850-3 at different stress levels under room temperature.

In the creep test of 850-3 (Figure S24), a stress of 1 MPa applied to the elastomer led to a strain of 13.7% at 25 °C. The release of stress over 10 min left a residual strain of less than 2.2%. The creep strain and residual strain after release increased with increasing applied stress. When the applied stress was up to 3 MPa, the creep strain and residual strain were 127.1% and 27.2%, respectively. The elastic deformation was instantaneously recovered, while the delayed elastic deformation and secondary creep recovered slowly due to time-dependent molecular relaxation.

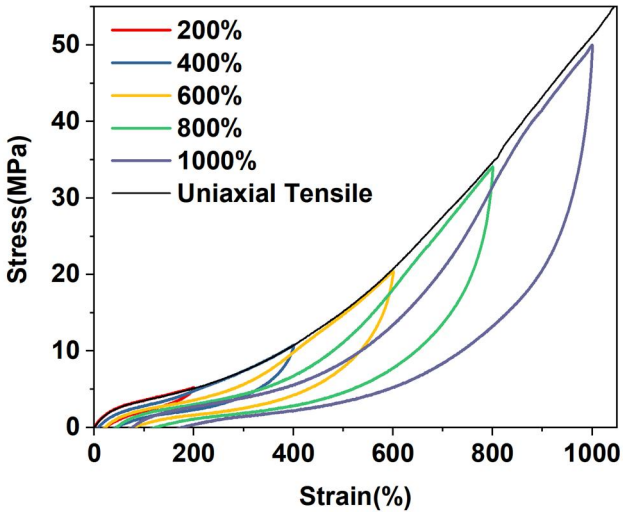

Figure S25. Cyclic loading–unloading tensile curves of the 850-3 at increasing strain.

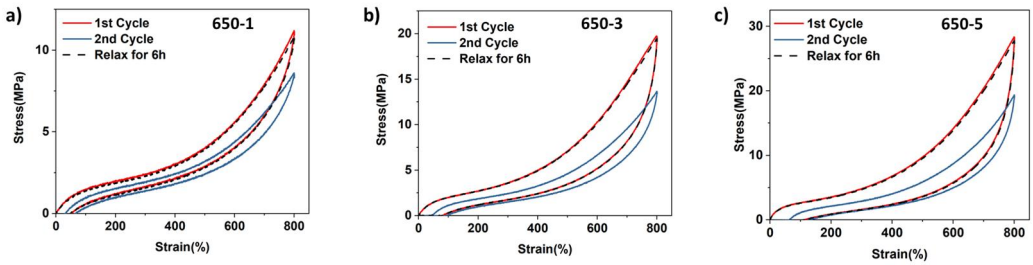

Figure S26. Large deformation cyclic tensile curves of (a)650-1, (b)650-3 and (c)650-5.

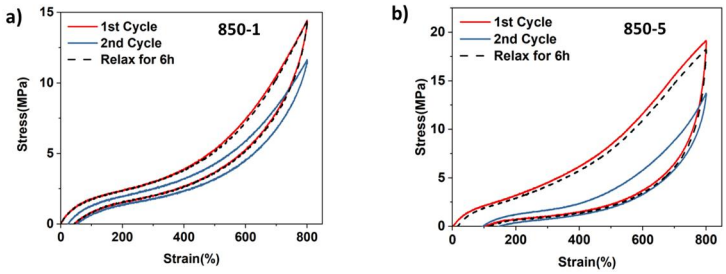

Figure S27. Large deformation cyclic tensile curves of (a)850-1 and (b)850-5.

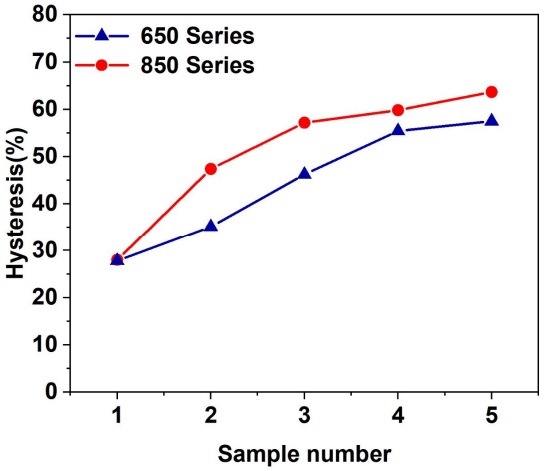

Figure S28. Energy dissipation ratio of 650 and 850 series.

As the sequence length increases, the hysteresis becomes more pronounced **(Figure S29)**. Among them, 650-1 and 850-1 exhibit small hysteresis (27.8% and 28.0%) while 650-5 and 850-5 show a large hysteresis (57.5% and 63.7%).

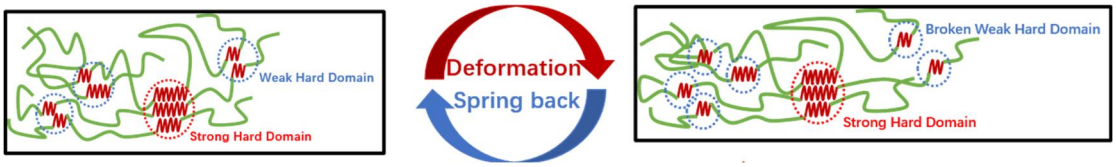

Figure S29. Illustration of rebound caused by coiling of the soft segments and reconstruction of the hard domains.

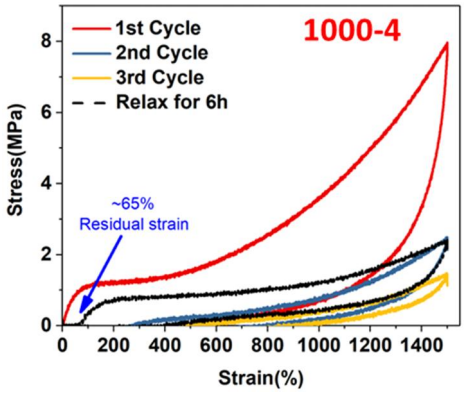

Figure S30. Large deformation cyclic tensile curves of 1000-4

In TPUs with microphase separation, the deformation process involves the destruction and orientation of the hard domains. At low strains, the soft domains deform synergistically, with the hard domains playing a prominent role in enhancing the modulus as physical crosslinking points. As the strain increases,

the weak hard domains start to break and release some of the locked soft segments, leading to a decrease in modulus (strain softening). Moreover, with further increase of the strain, the remaining hard domains as crosslinking points restrict the movement of molecular chains, resulting in an increase in stiffness (strain hardening). Therefore, with an increasing degree of microphase separation, more of the hard domains experience breakage during significant deformations, which cannot be quickly restored, ultimately leading to significant hysteresis and softening (Figure S26-28). However, when the strong hard domains are not completely destroyed during deformation, the original physical cross-linked network structure is thus maintained. As a result, the material slowly rebounds and the hard domains can be rebuilt after the load is removed. Figure S31 illustrates this process. Nevertheless, if the hard domains are severely damaged during deformation, the initial performance cannot be restored even after resting, as shown in the cyclic tensile curve of 1000-4 (Figure S30). Therefore, to achieve both high energy dissipation and low permanent deformation, it is crucial to strike a balance between the interplay of hydrogen bonding and breaking-reconstruction of the hard domains. Breaking and reformation of hydrogen bonds, along with the rupture of weak hard domains, contribute to increased energy dissipation. Conversely, the sufficient retention of strong hard domains helps reduce permanent deformation, although shape recovery may need some resting time.

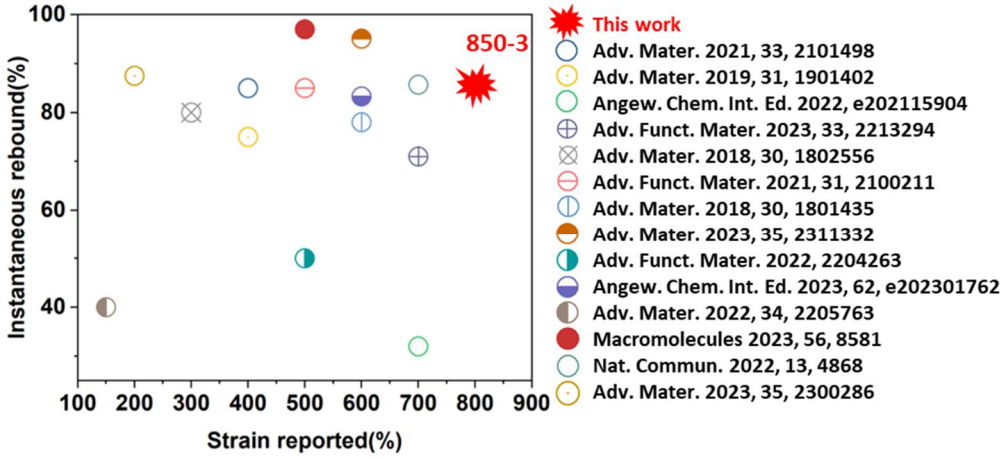

Figure S31. Comparison of instantaneous rebound ratio among 850-3 and other high-performance synthetic thermoplastic elastomers reported in recent literature. [2,3,12–14,4–11]

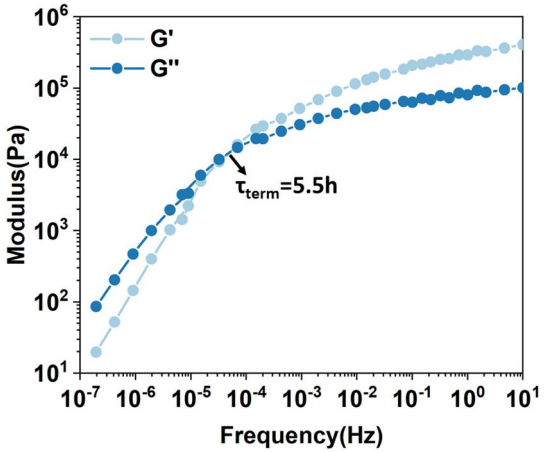

Figure S32. Master curves of frequency dependence of G′ and G″ for 850-3 at a reference temperature of 100 °C.

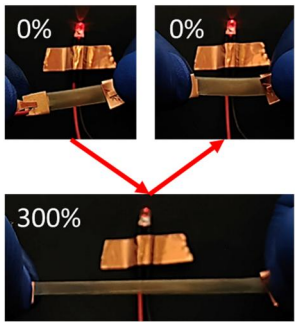

Figure S33. Images of the 850-3 IL50% at ~0% and ~300% strain connected in a circuit with an LED bulb.

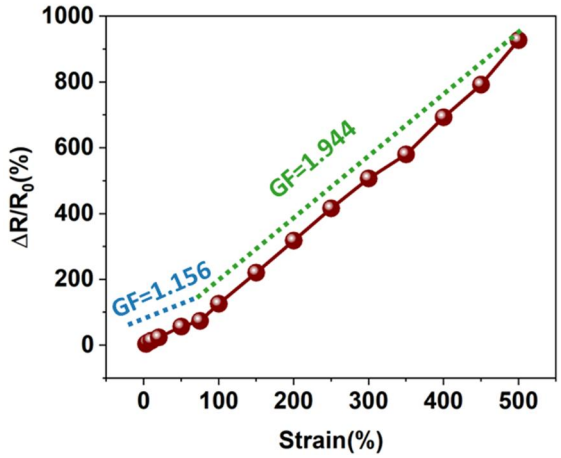

Figure S34. After being exposed to air for 1month, the relative resistance changes of 850-3 IL50% as a function of strain.

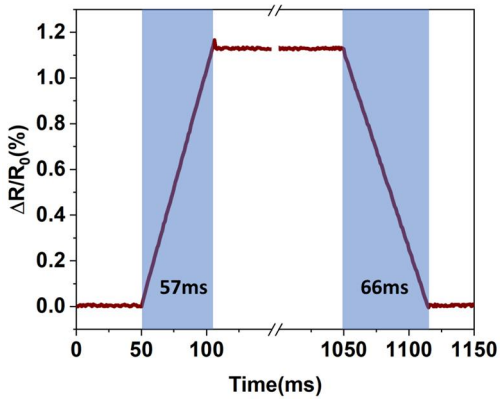

Figure S35. Response and relaxation time of 850-3 IL50% at 1% strain.

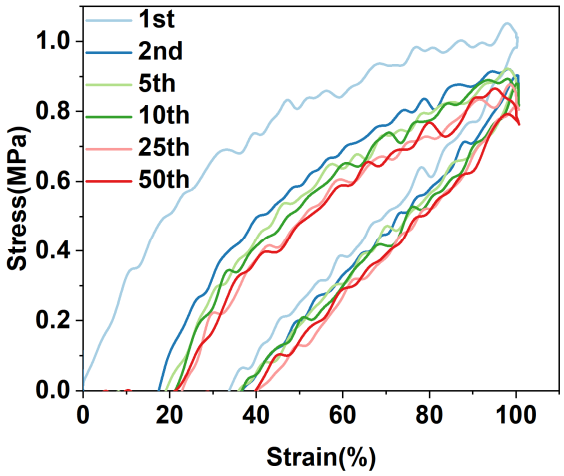

Figure S36. 50 successive loading-unloading cycles of 850-3 IL50%.

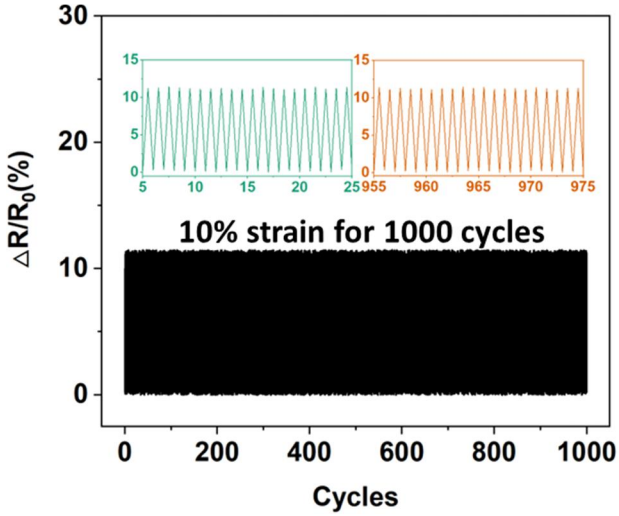

Figure S37. Cyclic stability tests of 850-3 IL50% under 10% strain for 1000 cycles.

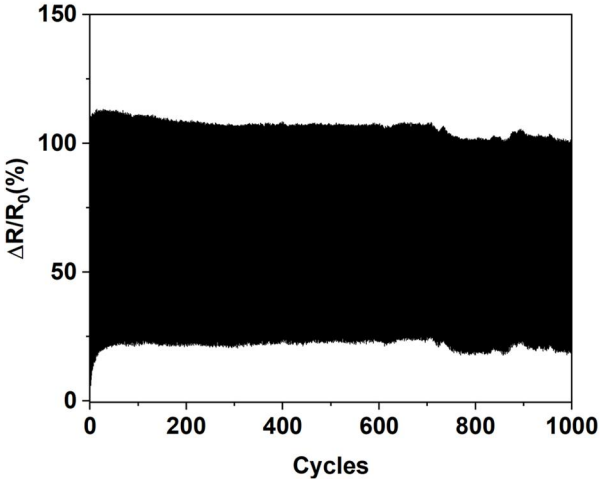

Figure S38. Cyclic stability tests of 850-3 IL50% under 100% strain for 1000 cycles.

References

1 S. Yiding and S. Mingshi, *China Synth. Resin Plast.*, 1990, **1**, 52–55.

2 Z. Li, Y. L. Zhu, W. Niu, X. Yang, Z. Jiang, Z. Y. Lu, X. Liu and J. Sun, *Adv. Mater.*, 2021, **33**, 2101498.
3 L. Zhang, Z. Liu, X. Wu, Q. Guan, S. Chen, L. Sun, Y. Guo, S. Wang, J. Song, E. M. Jeffries, C. He, F. L. Qing, X. Bao and Z. You, *Adv. Mater.*, 2019, **31**, 32–34.
4 S. R. Petersen, H. Prydderch, J. C. Worch, C. J. Stubbs, Z. Wang, J. Yu, M. C. Arno, A. V. Dobrynin, M. L. Becker and A. P. Dove, *Angew. Chemie - Int. Ed.*, 2022, **61**, e202115904.
5 Y. Lai, X. Kuang, P. Zhu, M. Huang, X. Dong and D. Wang, *Adv. Mater.*, 2018, **30**, 1802556.
6 W. Yao, Q. Tian, J. Shi, C. Luo and W. Wu, *Adv. Funct. Mater.*, 2021, **31**, 2100211.
7 Q. Zhang, S. Niu, L. Wang, J. Lopez, S. Chen, Y. Cai, R. Du, Y. Liu, J. C. Lai, L. Liu, C. H. Li, X. Yan, C. Liu, J. B. H. Tok, X. Jia and Z. Bao, *Adv. Mater.*, 2018, **30**, 1801435.
8 H. Chen, Z. Sun, H. Lin, C. He and D. Mao, *Adv. Funct. Mater.*, 2022, **32**, 2204263.
9 L. Wang, L. Guo, K. Zhang, Y. Xia, J. Hao and X. Wang, *Angew. Chemie - Int. Ed.*, 2023, **62**, e202301792.
10 X. Wang, J. Xu, X. Zhang, Z. Yang, Y. Zhang, T. Wang and Q. Wang, *Adv. Mater.*, 2022, **34**, 2205763.
11 J. Chen, Y. Gao, L. Shi, W. Yu, Z. Sun, Y. Zhou, S. Liu, H. Mao, D. Zhang, T. Lu, Q. Chen, D. Yu and S. Ding, *Nat. Commun.*, 2022, **13**, 4868.
12 Z. Guo, X. Lu, X. Wang, X. Li, J. Li and J. Sun, *Adv. Mater.*, 2023, **35**, 2300286.
13 H. Xiong, H. Wu, J. Zhang, S. Huang, S. Gu, Y. Hou, Q. Wu and J. Wu, *Macromolecules*, 2023, **56**, 8581–8591.
14 H. Chen, Z. Sun, K. Lu, J. Liu, C. He and D. Mao, *Adv. Mater.*, 2023, **35**, 2311332.